

# 3D Transition Metal Ordering and Rietveld Stacking Fault Quantification in the New Oxychalcogenides $\text{La}_2\text{O}_2\text{Cu}_{2-4x}\text{Cd}_{2x}\text{Se}_2$

Chris M. Ainsworth,<sup>(a)</sup> James W. Lewis,<sup>(a)</sup> Chun-Hai Wang,<sup>(a)\*</sup> Alan A. Coelho,<sup>(b)</sup> Hannah E. Johnston,<sup>(a)S</sup> Helen E. A. Brand,<sup>(c)</sup> John S. O. Evans<sup>(a,d)</sup>

<sup>(a)</sup>Department of Chemistry, University Science Site, Durham University, South Road, Durham, DH1 3LE, UK

<sup>(b)</sup> 72 Cedar Street, Wynnum, 4178 Brisbane, Australia

<sup>(c)</sup>Australian Synchrotron, 800 Blackburn Rd., Clayton, Victoria, 3168, Australia

<sup>(d)</sup>ANSTO (Australian Nuclear Science and Technology Organisation), New Illawarra Road, Rutherford Avenue, Lucas Heights, NSW 2234, Australia

---

**ABSTRACT:** A number of LnOCuCh (Ln = La–Nd, Bi; Ch = S, Se, Te) compounds have been reported in the literature built from alternating layers of fluorite-like  $[\text{Ln}_2\text{O}_2]^{2+}$  sheets and antiferrofluorite-like  $[\text{M}_2\text{Se}_2]^{2-}$  sheets, where M is in the +1 oxidation state leading to full occupancy of available  $\text{MSe}_{4/2}$  tetrahedral sites. There is also a family of related  $\text{LnOM}_{0.5}\text{Se}$  (Ln = La & Ce, M = Fe, Zn, Mn & Cd) compounds built from alternating layers of  $[\text{Ln}_2\text{O}_2]^{2+}$  sheets and  $[\text{MSe}_2]^{2-}$  sheets, where M is in the +2 oxidation state with half occupancy of available tetrahedral sites and complex ordering schemes in two dimensions. This paper reports a new family of compounds containing both +1 and +2 metal ions in the  $\text{La}_2\text{O}_2\text{Cu}_{2-4x}\text{Cd}_{2x}\text{Se}_2$  family. We show how  $\text{Cu}^{+1}$  and  $\text{Cd}^{2+}$  ions segregate into distinct fully occupied and half occupied checkerboard-like layers respectively, leading to complex long-range superstructures in the 3rd (stacking) dimension. To understand the structure and microstructure of these new materials we have developed and implemented a new methodology for studying low and high probability stacking faults using a Rietveld-compatible supercell approach capable of analyzing systems with thousands of layers. We believe this method will be widely applicable.

---

## INTRODUCTION

Mixed-anion materials display a wealth of fascinating exploitable properties based on their superconductivity, thermoelectric behaviour, optical properties, intercalation and ion-exchange chemistry, magnetism and others.<sup>1-14</sup> These properties are, of course, intimately related to their 3D structure and influenced by the specific architectures enforced or enabled by the simultaneous bonding requirements of different cation/anion combinations. We have previously described how combining rigid-geometry oxide building blocks with more flexible or adaptive chalcogenide layers can lead to infinitely adaptive structures with remarkable structural complexity (though governed by simple rules) in two dimensions.<sup>14, 15</sup> Here we show that this complexity can be extended to 3 dimensions in a new family of mixed metal oxychalcogenides. We unravel their crystal chemistry from powder diffraction studies, despite stacking faults leading to non-routine peak shapes. We show how it is possible to reproduce these complex experimental observations in a quantitative Rietveld approach using a simple two-parameter description across the entire structural series.

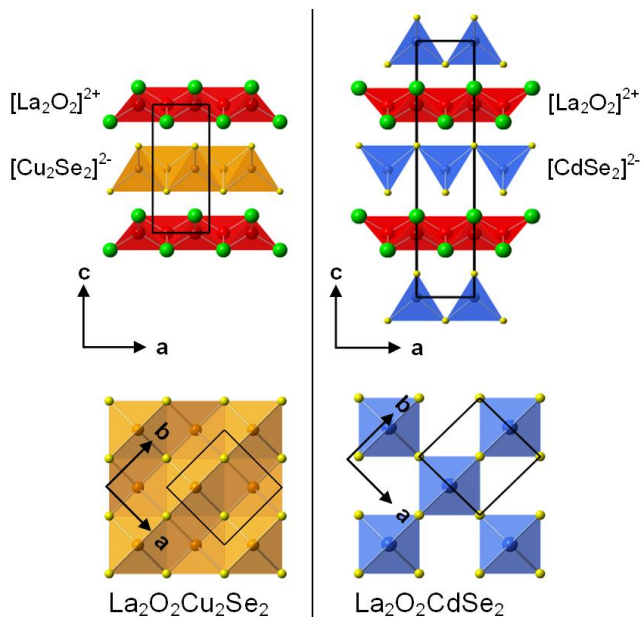


Figure 1. ZrCuSiAs-derived structures reported for (left)  $\text{La}_2\text{O}_2\text{Cu}_2\text{Se}_2$ ,  $P4/nmm$  symmetry, (right)  $\text{La}_2\text{O}_2\text{CdSe}_2$ ,  $P4/nmc$  symmetry. Top figures show the fluorite-like sheets of edge-sharing  $\text{Ln}_2\text{O}$  tetrahedra (red) and antifluorite-like sheets of  $\text{MSe}_4$  tetrahedra (orange/blue). Bottom figures are the view down  $[001]$ , showing the arrangement of  $\text{MSe}_4$  tetrahedra.  $\text{La}^{3+}$  cations are shown in green,  $\text{O}^{2-}$  anions in red,  $\text{Cu}^{+}$  cations in orange,  $\text{Cd}^{2+}$  cations in blue and  $\text{Se}^{2-}$  anions in yellow.

The compounds we report are structurally related to  $\text{LnOCuCh}$  ( $\text{Ln} = \text{La-Nd, Bi}$ ;  $\text{Ch} = \text{S, Se, Te}$ ) materials<sup>16, 17</sup> (though we use a doubled  $\text{La}_2\text{O}_2\text{Cu}_2\text{Ch}_2$  formula for convenience in most of the paper). These adopt the tetragonal ZrCuSiAs structure, space group  $P4/nmm$  (Figure 1, left). The structure is built up from alternating layers of fluorite-like  $[\text{Ln}_2\text{O}_2]^{2+}$  sheets and antifluorite-like  $[\text{Cu}_2\text{Ch}_2]^{2-}$  sheets. The oxidation state of Cu within these structures is +1, with full occupancy of available tetrahedral sites. These materials are of particular interest for their unusual optical/electronic properties combining high transparency and high electronic

conductivity. For example, the La compounds are wide band gap systems (3.1/2.8 eV for S/Se) with p-type conductivity up to  $910 \text{ Scm}^{-1}$ . The high conductivity arises from either Cu vacancies or Sr doping generating holes at the largely Cu  $3d/\text{Se } 4p$  derived valence band maximum.<sup>16-20</sup> Strong blue to UV emission is also observed and a room temperature blue emitting diode has been demonstrated.<sup>21</sup> Recently the low thermal conductivity and relatively high electrical conductivity of  $\text{BiOCuSe}$  ( $\sigma \sim 10 \text{ Scm}^{-1}$ ,  $\kappa = 1.0 \text{ Wm}^{-1}\text{K}^{-1}$ ) have created significant interest in thermoelectric applications and  $zT$  ( $= \frac{\alpha^2 \sigma}{\kappa}$ )  $T$  values up to 1.4 have been reported.<sup>5-7</sup> Perhaps the most famous compounds with this structure type are derived from  $\text{LaOFeAs}$ , and <sup>16-20</sup>superconduct at temperatures up to 55 K.<sup>1, 2</sup>

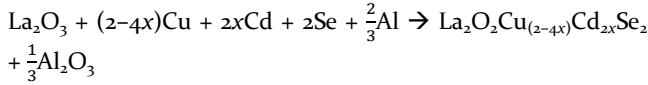
We and others have recently reported the structures of a range of related compounds containing 2+ metals, where charge balance leads to half the available metal sites in the tetrahedral layers being occupied and composition  $\text{Ln}_2\text{O}_2\text{MSe}_2$ .<sup>13-15, 22-27</sup> In the case of  $\text{M} = \text{Cd}$  this leads to the simple checkerboard (or  $Z_4^-$ ) ordering pattern of Figure 1 in which tetrahedra are exclusively corner-shared.<sup>23</sup> In other systems ( $\text{M} = \text{Fe, Mn, Zn, Cd}$  and combinations thereof) the high rigidity of the  $[\text{Ln}_2\text{O}_2]^{2+}$  layer can be used to tune the  $\text{M}^{2+}$  architecture from exclusively corner-sharing (e.g. La/Cd) to exclusively edge-sharing (e.g. Ce/Fe). Between these extremes we can generate compounds with different corner- to edge-sharing (C:E) integral ratios such as 5:1 (e.g. (Ce,La)/Mn), 4:1 (e.g. Ce/Zn), 3:1 (e.g. La/Zn) as well as incommensurate intermediate structures.<sup>14, 15</sup> As such we can prepare an infinitely adaptive series with large and complex superstructures in the  $ab$  plane.

In this work we report the synthesis and characterisation of the first  $\text{M}^{1+}/\text{M}^{2+}$  systems, the  $\text{LaOCu}_{1-2x}\text{Cd}_x\text{Se}$  or  $\text{La}_2\text{O}_2\text{Cu}_{2-4x}\text{Cd}_{2x}\text{Se}_2$  family. We again find a remarkable degree of long-range cation ordering, this time along the  $c$ -axis of the structure types shown schematically in Figure 2 for  $x = 0$  (all Cu) to  $x = 0.5$  (all Cd). As might be anticipated for layered materials with long-range periodicities, a variety of low-level stacking faults are suggested by the widths and asymmetry of weak superstructure peaks in the powder pattern that evidence this ordering. To provide full information on both the structure and microstructure of these materials has required development of a DIFFaX-like<sup>28</sup> approach to the treatment of stacking faults in a Rietveld refinement. We demonstrate for the first time that this approach is both possible and highly effective with models containing thousands of stacked layers and show how it leads to a simple description of the diffraction patterns of all the materials using two faulting probabilities.

Structure faults of this type are extremely common in a range of different materials and can have significant impact on their properties and function.<sup>29</sup> Examples include a wide range of battery materials<sup>30-36</sup>, zeolites<sup>37-44</sup>, metals<sup>45, 46</sup>, clays<sup>47, 48</sup>, diamond<sup>49, 50</sup>, ice<sup>50, 51</sup>, nitrides<sup>52-54</sup>, carbides<sup>55-57</sup>, catalysts<sup>58</sup>, layered hydroxides and other intercalation/ion-exchange hosts<sup>59-62</sup>. The Rietveld method we describe will be applicable to all these systems and will allow detailed and precise information to be obtained on the structure of individual phases and quantification of phase mixtures and their evolution *in operando*.

## EXPERIMENTAL SECTION

15 samples in the  $\text{La}_2\text{O}_2\text{Cu}_{2-4x}\text{Cd}_{2x}\text{Se}_2$  solid solution were prepared as polycrystalline powders. All samples were prepared according to the equation below, using the following reagents:  $\text{La}_2\text{O}_3$  (99.99%, Sigma Aldrich, heated to 1000 °C before use), Cu (99.9%, Alfa Aesar), Cd (99.5%, Alfa Aesar), Se (99.999%, Alfa Aesar), Al (99.5%, Alfa Aesar).



Reagents were intimately ground and placed in an alumina crucible. Al powder (10% molar excess) was placed in a second alumina crucible to act as an oxygen getter, forming  $\text{Al}_2\text{O}_3$  during the reaction. These two crucibles were placed in an evacuated ( $<10^{-3}$  atm) silica tube and slowly heated to a final dwell temperature of 1100 °C for 12 h, before cooling to room temperature.

For Rietveld analysis, X-ray data were collected on the powder diffraction beamline at the Australian synchrotron. Samples were loaded in a 0.3 mm capillary, and data collected using the Mythen microstrip detector from  $1 - 81^\circ 2\theta$  with a wavelength of 0.6354462(7) Å. To cover the gaps between detector modules, 2 datasets were collected with the detector set  $0.5^\circ$  apart and then merged to a single dataset using in-house data processing software, PDViPeR. Standard Rietveld refinements were performed using the Academic version of the TOPAS software.<sup>63-65</sup>

Stacking faults leading to broadening and asymmetry of peaks in the powder diffraction patterns were investigated

using a DIFFaX-like Rietveld approach in TOPAS. Details of the method are included in the Results and Discussion section. In brief, the crystal structure is described in terms of layers containing fixed blocks of atoms. These are stacked on top of each other in a supercell of the basic 9 Å cell of  $\text{La}_2\text{O}_2\text{Cu}_2\text{Se}_2$  using the format defined in the Topas manual.<sup>64</sup> This description allows significant simplification of structure factor calculations. The vectors describing possible transitions between layers and the probability rules for different layer-to-layer transitions are included in the TOPAS input file using a format similar to that of the DIFFaX software package. An external Python routine reads this information and produces a series of input files for Rietveld refinement in which stacking probabilities are systematically varied. The Python script submits each stack to TOPAS for Rietveld refinement and analyses and tabulates fault distributions and the model's fit to the diffraction data. A large number of different layer types can be stacked with up to six independent layer-to-layer probabilities  $pn$  which are expressed symbolically using the format  $pa$ ,  $pb$ ,  $1-pa$ ,  $1-pa-pb$ , etc, such that the sum of probabilities from any layer is 1.0. This gives sufficient flexibility to define a variety of different faults and memory effects. Recent speed enhancements made in Topas v6 mean that we could explore large supercells with low probability faults. We discuss investigations on supercells with up to 5000 layers, c-axis dimensions up to 35,000 Å and up to 28,000 atoms in the primitive unit cell. Note that despite the large number of atoms in a supercell description, the linking of coordinates between different layers means that complex structural descriptions are possible with a small (e.g. just one or two stacking fault probabilities) number of additional parameters.

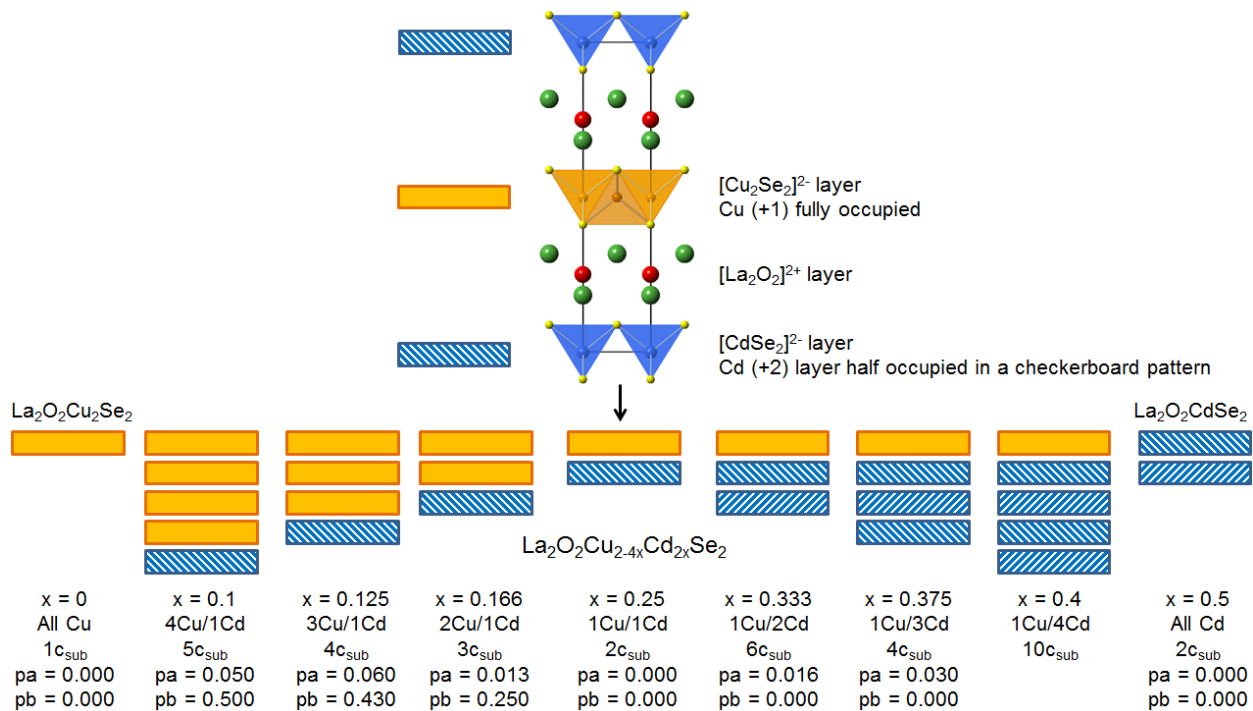


Figure 2. Schematic showing the unique crystallographic layers in samples prepared in the  $\text{La}_2\text{O}_2\text{Cu}_{2-4x}\text{Cd}_{2x}\text{Se}_2$  solid solution. The c axis length relative to a  $\text{Ln}_2\text{O}_2\text{Cu}_2\text{Ch}_2$  subcell model is shown along with the fraction of  $pa$  and  $pb$ -type faults present (discussed later in the text). Direction of blue hatching reflects different positions in the  $ab$  plane of Cd-centred tetrahedra.

## RESULTS & DISCUSSION

### Stacking Fault Methodology

The powder diffraction data of several of the new compounds described below showed significant *hkl*-dependence to peak widths and/or marked Warren-like<sup>66</sup> peak shapes which are suggestive of stacking faults.<sup>67</sup> Such faults are commonly found in layered materials, and whilst there have been various analytical and computational approaches to quantify them, readily accessible Rietveld-like approaches are limited. One implementation is the DIFFaX+ suite of Leoni et al. which places the Treacy, Newsam and Deem's DIFFaX algorithm in a least squares framework to allow refinement of stacking fault probabilities, though the approach is computationally demanding.<sup>68</sup> A second is the FAULTS approach of Casas-Cabanas *et al.*<sup>69</sup> To fully characterise our materials we have therefore developed and applied a DIFFaX-like<sup>28</sup> methodology for Rietveld refinement in the TOPAS suite which offers significant speed and flexibility advantages over previous approaches. It allows analysis of stacking faults alongside all the other features of TOPAS (multi-phase, multi-dataset, user-defined fitting functions and convolutions, parametric refinements, symmetry mode refinements, magnetism, etc). Our method builds on the supercell approach described by Ufer and co-workers<sup>47, 48, 70</sup> which has been applied in a Rietveld-like context for systems with a limited number of layers by Wang and Bette.<sup>71, 72</sup> In this method the structure is described in terms of a stack of individual layers in a supercell defined along the *c*-axis of the basic crystallographic cell. Individual layers in this supercell may differ in terms of chemical composition, internal structure or overall position in *x*, *y* or *z* relative to a reference layer. For a perfect or unfaulted stacking sequence the calculated pattern from the supercell will be identical to a conventional crystallographic subcell description (as all supercell reflections will have zero intensity). As faults are introduced into the stack, the superposition of multiple closely-spaced supercell reflections will sum to produce the complex peak shapes observed experimentally. By embedding this in a Rietveld package such as TOPAS, one can obtain simultaneous information about structure and microstructure of new materials. In our implementation the probabilities *pn* of layer-to-layer transitions are defined using a probability matrix of the format defined in the DIFFaX software package of Treacy et al.<sup>28</sup> A python routine reads this matrix and produces an input file suitable for Rietveld refinement in TOPAS. For structures containing layers of different chemical composition the user can control the overall composition.

One of the major issues with this approach has been the size of the supercell that can be used. There are many potential advantages of using a large supercell: low probability stacking faults can be identified, the closely-spaced *hkl* reflections better approximate the continuous diffuse scatter expected in reciprocal space, and an individual supercell description is likely to be a good statistical approximation of the ensemble of different crystallites contributing to the powder pattern. There are, however, significant computational bottlenecks associated with calculating the powder pattern from a large supercell, in particular the large number of reflections that must be summed to produce the calculated pattern,  $y_{\text{calc}}$ . In previous work this has required handling *ool* and *hko* reflections separately for turbostratic systems,<sup>47, 48</sup> or the use of relatively small supercells to approximate materials.<sup>71, 72</sup> In

this work we have introduced new approximations to the Rietveld method which circumvent this problem. The most significant of these impacts the peaks buffer. TOPAS uses a peaks buffer for computational efficiency when calculating peak shapes over a defined narrow  $2\theta$  range. Peak shapes only need to be calculated for reflections at the start and end of a  $2\theta$  range; these end peaks are then interpolated or stretched to realize intervening peaks, leading to significant speed gains. Peaks invariably comprise the convolution of instrument and sample aberrations with the emission profile to form the final peak shape. The number of peaks stored in the peaks buffer (or the number of  $2\theta$  ranges needed to fit the whole pattern) is determined by looking at allowed changes in these aberrations as a function of  $2\theta$ . When changes exceed predefined limits a new  $2\theta$  range is created. These predefined aberration limits can be modified but in practice this is rarely done due to the complexity of the procedure. In cases where aberrations are *hkl* dependent, anisotropic peak broadening for example, TOPAS traditionally eliminates the peaks buffer and instead a new peak is calculated for each reflection regardless of any similarities in peak shapes. This process works well in typical Rietveld refinements where a few hundred to maybe a few thousand reflections are present.

In the present work, supercells can result in hundreds of thousands to even millions of *hkl* reflections each potentially having a unique peak shape due to a *hkl*-dependent aberration. To speed up the process TOPAS now allow tolerances to be defined at the parameter level with subsequent peak groupings handled automatically. Parameters can, for example, correspond to peak positions, peak widths or even the magnitude of any *hkl* dependent function. Multiple criteria can be used where peak groups can be further subdivided. The net result is that a whole pattern can be described using hundreds rather than thousands of thousands of peaks.

An additional speedup in calculation comes at the stage where the reduced number of peaks is summed onto the diffraction pattern. For a sequence of closely-spaced *hkl* reflections belonging to a particular group the peak intensities are apportioned to a pair of *hkl* reflections at the start and end of the sequence. The final result is the ability to synthesise diffraction patterns in a fraction of the time with little or no loss in precision, allowing Rietveld refinement with very little impact on the fit quality or the derived parameters. Of equal importance is the reduction in computer memory usage realized through the reduction in the size of the peaks buffer; Rietveld refinement without such a reduction in memory would not otherwise be possible.

As an illustration of this approach we used the test input file *dia.dat* distributed with the DIFFaX suite to calculate the expected powder pattern for a sample of stacking-faulted diamond containing intergrowths of the cubic diamond and hexagonal lonsdaleite forms with a 0.7 probability (*pa*) of ideal *c-c* and *h-h* stacking and a 0.3 probability (*1-pa*) of *h-c* or *c-h* faults. This example is discussed in the literature and produces the complex peak shapes shown in Figure 3.<sup>28</sup> These simulated data were then fitted using our Rietveld approach with a supercell containing 5000 carbon layers and unit cell parameters of  $2.518 \times 2.518 \times 10292 \text{ \AA}^3$ , giving a total of 236884 predicted *hkl* reflections from  $10$  to  $150^\circ 2\theta$ . As described in the DIFFaX manual, this cell is a superstructure of the hexagonal setting of the diamond cell, with a 5000  $\times$

2.05859 Å supercell along the  $c$ -axis (parallel to  $[111]$  of the cubic cell). Using the peaks buffer approach the pattern could be well approximated using just 285  $hkl$  reflections with no change in  $R_{wp}$ . Figure 3a shows the Rietveld fit for this model using just 7 refined parameters (1 scale, 2 isotropic peak shape parameters, 4 background terms) for a faulting probability of  $pa = 0.7$ . An excellent agreement is observed between the simulated data and the Rietveld fit, and the complex peak shapes are extremely well reproduced.

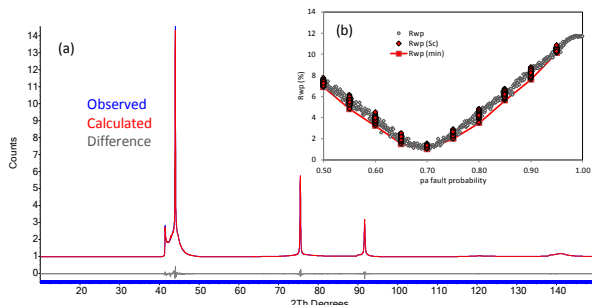


Figure 3. (a) Stacking mode Rietveld fit to a DIFFaX-simulated powder pattern of faulted cubic/hexagonal diamond. 5000 layers with a fault probability of 0.7 give excellent agreement to the simulated data. The blue “bar” at the bottom of the figure represents tick markers for each of the 236884  $hkl$  reflections predicted over this  $2\theta$  range. (b) Dependence of  $R_{wp}$  on  $pa$ . Grey open points are a series of stacks with different  $pa$ ; closed red points are a series of 100 repeat stacks at discrete  $pa$  values.

Figure 3b shows the Rietveld agreement factor  $R_{wp}$  as the stacking fault probability  $pa$  is systematically varied from 0.5 to 1.0. A clear minimum in  $R_{wp}$  is found at  $pa = 0.7$  showing that the fault probability can be well quantified for this system. To produce this figure two methods were used. In a first run 500 models were tested as  $pa$  was changed in steps of 0.01. In a second run, 50 repeat stacks were analysed at  $pa$  values from 0.50 to 0.95 in 0.05 steps. The vertical scatter in  $R_{wp}$  above the minimum therefore gives an indication of how different stacks produced using the same stacking probability influence  $R_{wp}$ . The scatter in  $R_{wp}$  (standard deviation 0.1 close to the  $pa$  minimum) shows that a 5000 layer stack gives a good statistical model for the infinite stack simulated by DIFFaX. These calculations can be performed rapidly on a modest PC. On an i7 3.4 GHz single core desktop computer each Rietveld cycle took  $<0.35$  s with a peak memory use of 110 Mb such that the 1000 repeat refinements of Figure 3(b) took around 3 hours. Without the peaks buffer improvements 2.9 Gb of memory is needed even for this simple system and cycles are 10 times slower.

Using fewer layers in the Rietveld model gives an increase in the  $R_{wp}$  spread, but the minimum remains reasonably defined even with only 100 layers. The increased spread of  $R_{wp}$  arises due to the different superstructure peak intensities from different specific layer sequences in the stacks. When investigating low probability faults in small stacks it is important to fit multiple stacks generated with a given set of transition probabilities to the diffraction data. The best fit to the data is typically achieved by averaging the calculated patterns of multiple models to better represent the ensemble of crystallites in a sample.<sup>67</sup> This approach was applied to the different  $\text{La}_2\text{O}_2\text{Cu}_{2-4x}\text{Cd}_x\text{Se}_2$  phases prepared in this work.

## New $\text{La}_2\text{O}_2\text{Cu}_{2-4x}\text{Cd}_x\text{Se}_2$ Materials

Samples across the  $\text{La}_2\text{O}_2\text{Cu}_{2-4x}\text{Cd}_x\text{Se}_2$  solid solution were synthesized over 12 h at 1100 °C with an aluminium oxygen getter to control oxygen composition.  $\text{La}_2\text{O}_2\text{Cu}_2\text{Se}_2$  and  $\text{La}_2\text{O}_2\text{CdSe}_2$  were colored khaki and sienna respectively, while all other samples were yellow-ochre. These colors are shown visually in the Supporting Information (SI) as Table S1.

Powder X-ray diffraction data showed that in all cases, layered ZrCuSiAs-related phases had formed with a unit cell  $a = b \approx 4$  Å,  $c \approx 9$  Å (the subcell), explaining the main peaks present. Weak additional reflections were observed at low angles for all samples (with the exception of  $\text{Ln}_2\text{O}_2\text{Cu}_2\text{Ch}_2$ , where full occupancy of the Cu site gives no supercell reflections), which could not be attributed to known impurity phases. It is shown below that these arise from transition metal ordering. The layered phases account for  $>98.5\%$  weight percentage in all the new compounds prepared, with a minor  $\text{La}_2\text{O}_2\text{Se}$  impurity. Table S2 gives the weight percentages of the phases formed for all samples.

Unit cell volumes (Figure 4) showed a smooth variation across the series suggesting a smooth change in structure with composition. The  $a$  cell parameter remains relatively unchanged across the series (see Figure S1) whilst the  $c$ -axis expands rapidly. As in related materials, this shows the high rigidity of  $\text{Ln}_2\text{O}_2$  layers relative to  $\text{M}_n\text{Se}_2$  layers. The compositions we discuss in detail below contained a single layered phase (the red points of Figure 4). For some other compositions we see evidence of phase segregation. For example at a nominal  $x = 0.45$  we see three similar layered phases with cell volumes corresponding to  $x = 0.4$ ,  $x = 0.46$  and  $x = 0.5$  in a  $\sim 5:14:1$  ratio as indicated by the three vertical grey points for this nominal composition. This implies an inherent stability of the ordered structures shown in Figure 2 and discussed below.

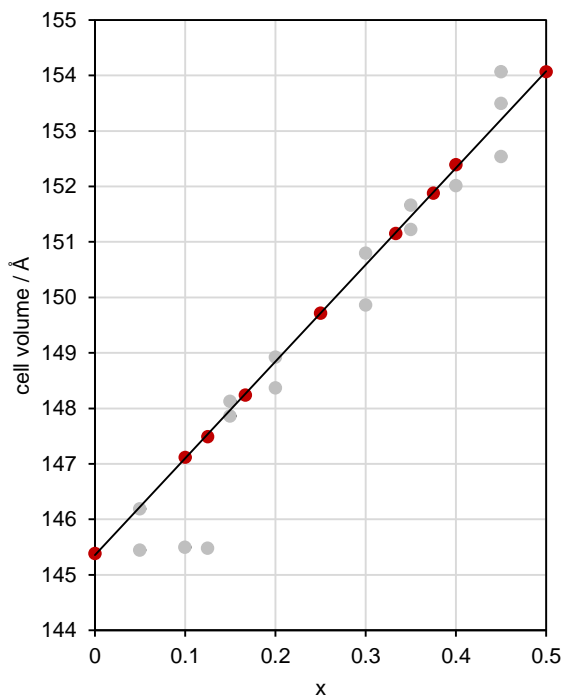


Figure 4. Variation in cell volume of phases formed across the  $\text{La}_2\text{O}_2\text{Cu}_{2-4x}\text{Cd}_x\text{Se}_2$  solid solution. Red and grey circles are explained in the text.

### $x = 0$ (all Cu) and $x = 1$ (all Cd)

$\text{La}_2\text{O}_2\text{Cu}_2\text{Ch}_2$  and  $\text{La}_2\text{O}_2\text{CdSe}_2$  end members were synthesized and diffraction data were fully consistent with the structures previously reported in the literature and shown in Figure 1. PXRD data are included in Figure 12. Minor (2%) impurities are present in the Cd end member under these synthetic conditions. Fully pure samples can be made at 950K<sup>23</sup>. For this work we deliberately chose a single set of synthesis conditions for all compositions.

### $x = 0.25$ $\text{La}_2\text{O}_2\text{CuCd}_{0.5}\text{Se}_2$ (1Cu/1Cd layer)

Synchrotron data of the  $x = 0.25$  composition showed that a layered ZrCuSiAs-related phase had formed with a unit cell  $a = b = 4.07 \text{ \AA}$ ,  $c = 9.05 \text{ \AA}$  (the subcell), explaining the main peaks present. Figure 5a shows a  $\text{La}_2\text{O}_2\text{Cu}_2\text{Se}_2$  model,  $P4/nmm$  (red) refined against the experimental data (blue). Weak additional reflections are clearly observed. Figure 5b shows a refined  $\text{La}_2\text{O}_2\text{CdSe}_2$  model, space group  $P4_2/nmc$ , which fits some, but not all of the supercell reflections.

The ionic radii of  $\text{Cu}^{1+}$  and  $\text{Cd}^{2+}$  ions differ considerably; Shannon's tables give values of 0.6 and 0.78  $\text{ \AA}$  for  $\text{Cu}^{1+}$  and  $\text{Cd}^{2+}$  respectively.<sup>73</sup> Models were therefore investigated which have Cu and Cd in distinct layers. If this occurs, a sample with composition  $\text{La}_2\text{O}_2\text{CuCd}_{0.5}\text{Se}_2$  would need to have a 1:1 ratio of  $\text{Cu}^{1+}$  layers (fully occupied) to  $\text{Cd}^{2+}$  layers (half occupied). Perhaps the most likely structural model of this sort would have alternating Cu and Cd layers, with the Cd occupying alternate checkerboard sites either side of a given Cu layer. This model is shown in Figure 6 (left), and would have space group  $P4_2/nmc$ . Figure 5c shows this model refined against the experimental data, but it is clearly incorrect.

A second possible model would also have alternating Cu and Cd layers, but with the Cd occupying the same sites either side of a given Cu layer, shown in Figure 6 (right), space group  $P-4m2$ . Figure 5d shows this model refined against the experimental data. It provides an excellent fit. Full crystallographic details of the final model (and other refinements in the paper) are included as Table S3.

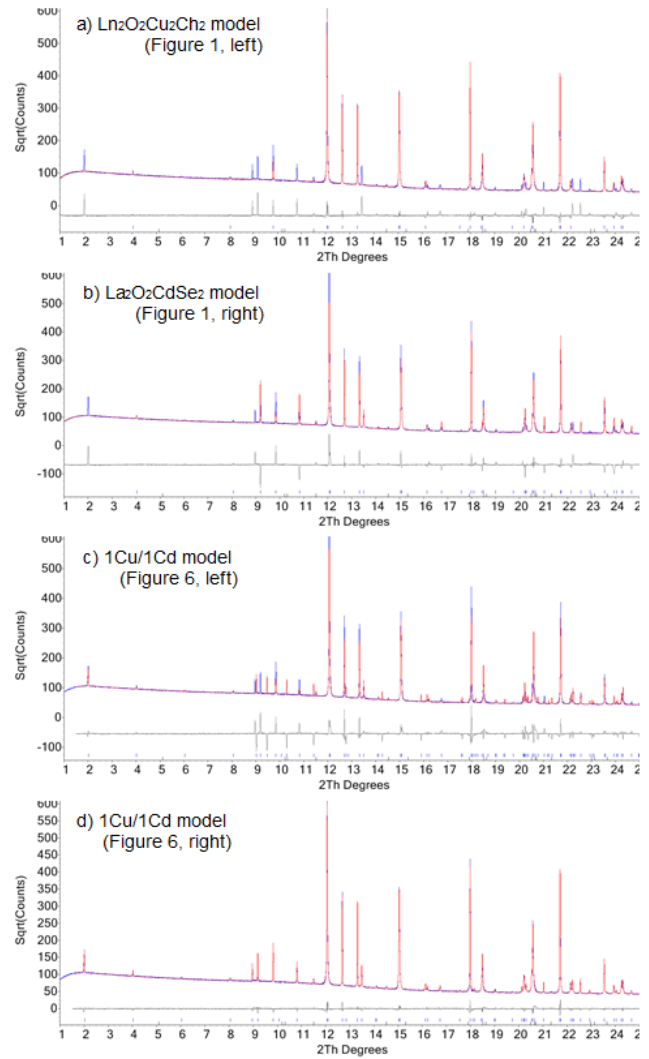


Figure 5. Rietveld refinement profiles of synchrotron powder diffraction data for  $\text{La}_2\text{O}_2\text{CuCd}_{0.5}\text{Se}_2$  using the structural models discussed in the text. The correct model is that given in Figure 6, right. A  $\sqrt{I}$  scale is used to emphasize the weaker supercell reflections.

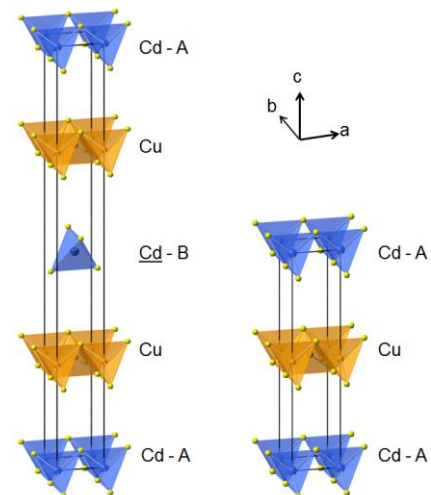


Figure 6. Two possible structural models for  $\text{La}_2\text{O}_2\text{CuCd}_{0.5}\text{Se}_2$  with alternating layers of Cu and Cd. The model with Cd occupying equivalent sites either side of a Cu layer (right) is the correct model.  $\text{Cu}^{1+}$  cations are shown in orange,  $\text{Cd}^{2+}$  cations in blue and  $\text{Se}^{2-}$  anions in yellow.  $[\text{La}_2\text{O}_2]^{2+}$  layers are omitted for clarity.

**Cd-rich samples:  $x = 0.333, 0.375, 0.4, 0.45$  (1Cu/2Cd, 1Cu/3Cd, 1Cu/4Cd, 1Cu/9Cd)**

Compounds expected to contain more Cd than Cu layers were investigated for  $x = 0.333, 0.375, 0.4$  and  $0.45$ . In all cases the formation of  $\text{La}_2\text{O}_2\text{Cu}_x\text{Se}_2$ -derived phases was clear from powder diffraction data. For  $x = 0.333$  a model was constructed with a 1:2 ratio of Cu:Cd layers, with Cd occupying equivalent sites either side of a given Cu layer as suggested by the  $x = 0.25$  structure, and opposite sites when in adjacent layers as found in  $\text{La}_2\text{O}_2\text{CdSe}_2$  (Figure 7a) This leads to space group  $P4_2/nmc$ .

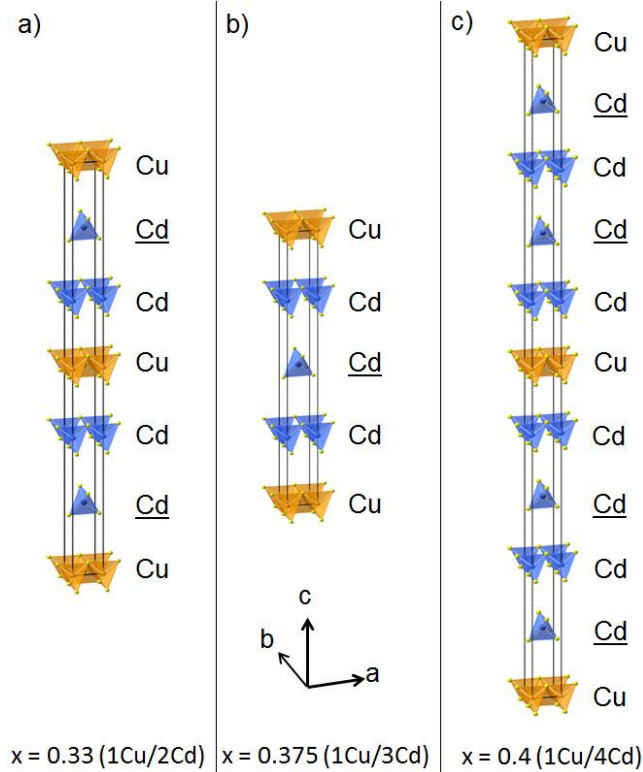


Figure 7. Structural models for (a)  $\text{La}_2\text{O}_2\text{Cu}_{0.66}\text{Cd}_{0.66}\text{Se}_2$  (1Cu/2Cd), (b)  $\text{La}_2\text{O}_2\text{Cu}_{0.50}\text{Cd}_{0.75}\text{Se}_2$  (1Cu/3Cd) and (c)  $\text{La}_2\text{O}_2\text{Cu}_{0.40}\text{Cd}_{0.80}\text{Se}_2$  (1Cu/4Cd), space group  $P4_2/nmc$ ,  $P-4m2$  and  $P4_2/nmc$  respectively.  $\text{Cu}^{+}$  cations are shown in orange,  $\text{Cd}^{2+}$  cations in blue and  $\text{Se}^{2-}$  anions in yellow.  $[\text{La}_2\text{O}_2]^{2+}$  layers are omitted for clarity.

On initial inspection, the refined model seems to provide a satisfactory fit to experimental data (Figure 8a), with  $R_{wp} = 5.92\%$ . However, upon closer inspection, several of the weak supercell peaks show minor discrepancies in both peak intensity and widths (Figure 8b, peaks marked with arrows). Note that Figure 8 is drawn with a  $\sqrt{I}$  scale such that these reflections are  $\sim 0.25\%$  of the strongest subcell reflections.

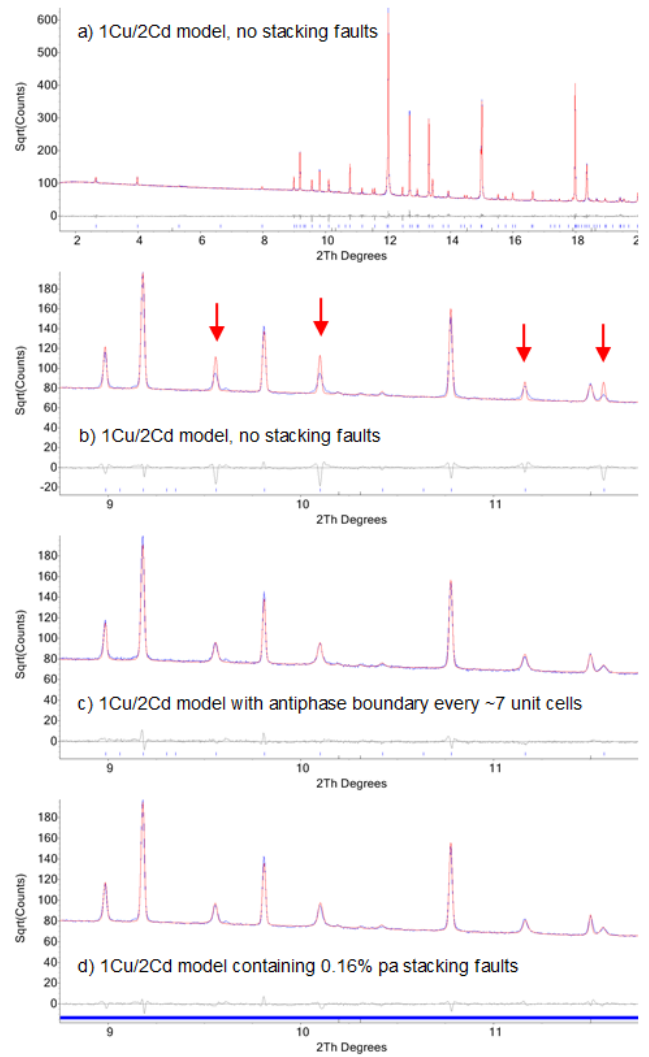


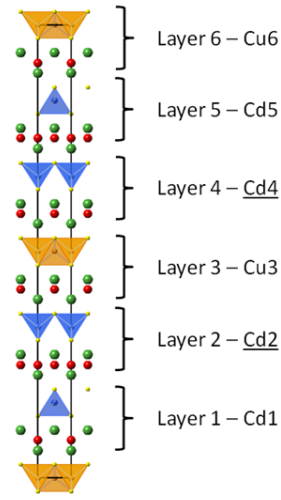
Figure 8. Rietveld refinement profiles of synchrotron powder diffraction data for  $\text{La}_2\text{O}_2\text{Cu}_{0.66}\text{Cd}_{0.66}\text{Se}_2$  using the structural model proposed in Figure 7a, both without and with stacking faults. The correct model contains  $\sim 0.16\%$  pa stacking faults. A  $\sqrt{I}$  scale is used to emphasize the weaker supercell reflections.

Analysis of individual reflections showed a clear broadening of all  $hkl$  reflections where  $l \neq 3n$ . Therefore, an additional parameter was introduced to model antiphase domain walls perpendicular to  $c^*$ , using the approach employed in the refinements of  $\text{MgB}_2\text{H}_8$ <sup>74</sup>, but with an  $l = 3n$  condition. This leads to an improved fit of supercell reflections (Figure 8c),  $R_{wp} = 5.01\%$ , and refined fault domain size value of  $\sim 380$  Å suggesting the presence of a fault every  $\sim 7$  unit cells (42 layers).

Since the other members of the  $\text{La}_2\text{O}_2\text{Cu}_{2-4x}\text{Cd}_x\text{Se}_2$  series show more complex broadenings of the supercell reflections, we have applied our DIFFaX-Rietveld approach to these data. The alternating  $[\text{La}_2\text{O}_2]^{2+}$  and either  $[\text{CdSe}_2]^{2-}$  or  $[\text{Cu}_2\text{Se}_2]^{2-}$  2D units in these structures mean that we can easily describe the structure in terms of  $[\text{LaOLaSe}(\text{Cu}_2/\text{Cd})\text{Se}]$  layers stacked along  $c$  and that two types of stacking fault are likely for  $x = 0.33$  (Figure 9). Firstly one could break the (Cu|Cd|Cd) repeat by introducing an additional layer of either metal to form (Cu|Cu|Cd|Cd) or (Cu|Cd|Cd|Cd) local faults. We call this a *pa*-type fault throughout the paper. These correspond to a local intergrowth of  $x = 0.25$  and  $x = 0.375$  phases, and

chemical composition requirements mean that their number must be balanced. The cell volume plot of Figure 4 and single-phase nature of this sample provide strong evidence that the composition is that expected.

A second possibility is a fault of the type shown in Figure 6, left, where neighboring Cd atoms layers are offset by  $\pm(a/2, b/2)$  in the  $ab$  plane across a Cu layer. We call this a  $pb$ -type fault. The structure of faulted  $x = 0.33$   $\text{La}_2\text{O}_2\text{Cu}_{0.66}\text{Cd}_{0.66}\text{Se}_2$  can then be described by stacking 6 layers labelled  $\text{Cd}_1$ ,  $\underline{\text{Cd}_2}$ ,  $\text{Cu}_3$ ,  $\underline{\text{Cd}_4}$ ,  $\text{Cd}_5$ , &  $\text{Cu}_6$  as shown in Figure 5, with transition probabilities from layer to layer as defined in the accompanying probability matrix. In this description an underlined Cd atomic layer is offset by  $(a/2, b/2)$ . The ideal structure is generated by stacking  $(\text{Cd}_1|\underline{\text{Cd}_2}|\text{Cu}_3|\underline{\text{Cd}_4}|\text{Cd}_5|\text{Cu}_6)_\infty$ . A  $pa$  type fault can be introduced by an  $m \rightarrow m+3$  transition and a  $pb$  fault by  $\text{Cu}_3 \rightarrow \text{Cd}_1$  or  $\text{Cu}_6 \rightarrow \underline{\text{Cd}_4}$ . In this description a  $pa$  fault after a Cd layer retains the Cd offset pattern observed in  $\text{La}_2\text{O}_2\text{CdSe}_2$  and a  $pa$  fault after a Cu layer leads to Cd's retaining the  $xy$  position they would have within a given layer in an unfaulted stack; by setting  $pa$  to an  $m \rightarrow m$  transition for Cu layers the alternate fault in which Cd position is mirrored across a  $pa$ -induced Cu double layer can be explored.



		from layer $m$					
to layer $n$		0	0	$pb$	$pa$	0	$1 - pa - pb$
		$1 - pa$	0	0	0	$pa$	0
		0	$1 - pa$	0	0	0	$pa$
		$pa$	0	$1 - pa - pb$	0	0	$pb$
		0	$pa$	0	$1 - pa$	0	0
		0	0	$pa$	0	$1 - pa$	0

Figure 9. Layer description and stacking probability matrix for  $x = 0.33$ . Each  $pa$  fault retains the Cd offset that would be adopted in an ideal stack.

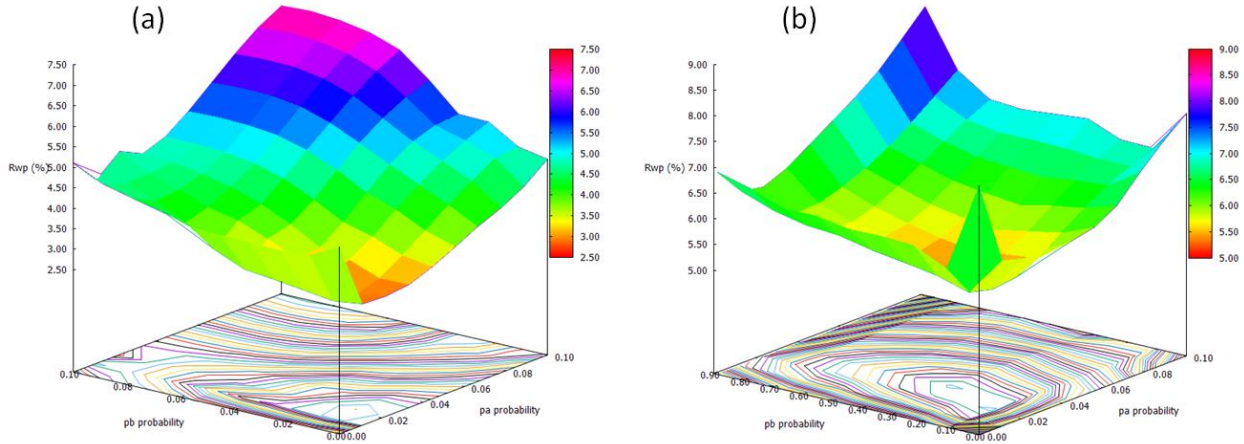


Figure 10. Dependence of  $R_{wp}$  on  $pa$  and  $pb$  for the  $x = 0.33$  and  $x = 0.167$  systems. Note different  $pb$  scale in (b).

The supercell was constructed by stacking 320 Cu and 640 Cd layers with internal geometries derived from the  $x = 0.125$  refinement. The ideal thickness of each layer type along the  $c$  axis can be estimated from the  $c$  cell parameter in  $x = 0$  (Cu) and  $x = 0.5$  (Cd) series end members as  $8.7975 \text{ \AA}$  and  $9.3160 (=18.6320/2) \text{ \AA}$  respectively. The thickness defines the displacement along  $c$  from one layer to the next. For rigid layers, the supercell should then have a  $c$  axis of  $320 \times 8.7975 \text{ \AA} + 640 \times 9.3160 \text{ \AA} = 8777.44 \text{ \AA}$ , implying a subcell parameter of  $9.1432 \text{ \AA}$ . Experimentally the subcell parameter is  $9.1410(3) \text{ \AA}$ , so ideal thicknesses were automatically scaled during the refinement to account for this very small discrepancy. This supercell model gave a good fit to the diffraction data with an  $R_{wp}$  only marginally higher than a standard crystallographic model (4.1 vs 3.9 % for  $2-20^\circ 2\theta$ ), despite having no refined structural parameters. Our peaks-buffer approach

means that the pattern is simulated using 1530  $hkl$  reflections rather than the 54881 predicted for this supercell size and  $2\theta$  range. As expected, an identical  $R_{wp}$  is obtained for any unfaulted supercell containing  $6n$  layers. A grid search was then performed with both  $pa$  and  $pb$  allowed to vary from 0 to 0.1 and 100 trial stacks tested for each  $pa/pb$  pair (approximately 15 hours of computer time). Analysis of the  $R_{wp}$  surface (Figure 10) indicated a significant improvement in fit ( $R_{wp} = 2.78 \%$ ) for structures with  $\sim 18$   $pa$  faults in the stack and no  $pb$  faults, corresponding to a fault every  $\sim 490 \text{ \AA}$  or 54 layers. As shown in Figure 8d, this model reproduces the shape and intensities of weak supercell reflections extremely well, with only one additional structural parameter ( $pa$  value). Refinement of parameters defining the relative thickness of Cu/Cd layers gave essentially no change in  $R_{wp}$  and refined values of  $8.806/9.307 \text{ \AA}$ . We also investigated models

with imposed correlation lengths between faults but found that the best fits had uncorrelated faults. As well as the “extra layer” *pa* model we investigated a similar “missing layer” *pc* fault. We find that similar fits to the data are possible with either fault type, but that their sum remains constant.

Rietveld fits for the  $x = 0.375$  composition are included later in Figure 12. The powder diffraction data are essentially consistent with the structural model shown in Figure 7b, which contains blocks of 3 Cd’s, within which the structural arrangement is the same as in  $\text{La}_2\text{O}_2\text{CdSe}_2$ , followed by a Cu layer. This model, however, significantly overestimates the intensity of the weak 002 and 003 reflections at  $\sim 2$  and  $\sim 3^\circ 2\theta$  as well as, for example, the  $01l \neq 2n$  reflections. A *pa/pb* grid search similar to that for the  $x = 0.33$  sample was investigated and a significant reduction in  $R_{\text{wp}}$  (5.81 to 2.78 %,  $2-20^\circ 2\theta$ ) was achieved with approximately 25 *pa* faults. Introduction of *pb* faults caused an increase in  $R_{\text{wp}}$ . Refinement of the Cu/Cd slab thickness gave 8.861/9.248 Å, close to expected values.

Inspection of the powder data for  $x = 0.4$  and  $x = 0.45$  suggests similar basic structures with a  $(\text{Cu}|\text{Cd}|\text{Cd}|\text{Cd}|\text{Cd})_\infty$  repeat for  $x = 0.4$ , and similar *pa* type faults. The weak intensity of the superstructure peaks and the likelihood of partial phase separation precludes detailed analysis of the stacking faults. For  $x = 0.45$  we see evidence for partial phase segregation to  $x = 0.4$  and  $x = 0.5$  compositions.

**Cu-rich samples:  $x = 0.167, 0.125, 0.1, 0.05$  (2Cu/1Cd, 3Cu/1Cd, 4Cu/1Cd, 9Cu/1Cd)**

From powder diffraction data we can identify 3 new discrete structure types for Cu-layer-rich compositions. The basic structure types found are depicted in Figure 11, though we again see marked supercell peak broadening and significant peak asymmetry. For  $x = 0.167$  the supercell reflections are well fitted with *pa*  $\approx 0.013$  suggesting a similar number of layer-repeat faults to the Cd-rich phases. There are also a significant number of *pb*-type faults (*pb*  $\approx 0.25$ ) corresponding to 80 faults in the 960 layer stack, or a fault every 55 Å or 6 layers. The dependence of  $R_{\text{wp}}$  on *pa* and *pb* is given in Figure 10b. As the number of Cu layers is increased, the proportion of *pb*-type faults increases. At  $x = 0.125$  (Cu|Cu|Cu|Cd) *pb* is  $\approx 0.43$  implying an almost-random choice for the position of the Cd layers. This leads to the triangular or Warren-like peak shape seen for the  $10l$ -related peaks from  $\sim 8.9^\circ 2\theta$ , shown in Figure 12. This sample also contains a significant number of *pa* type defects (*pa*  $\approx 0.06$ ). Without these defects *ool* reflections have too high a peak height. In a conventional crystallographic refinement using an average model this effect is partially “mopped up” by the thickness of Cd and Cu layers distorting.

For  $x = 0.1$  we find *pb* = 0.5 gives the best fit to the data (Figure 11e) implying full disorder of the Cd atoms over the two sites available. For  $x = 0.05$  (targeted to be 9Cu/1Cd), phase separation is observed, into  $x = 0.05$  and  $x = 0$  compositions.

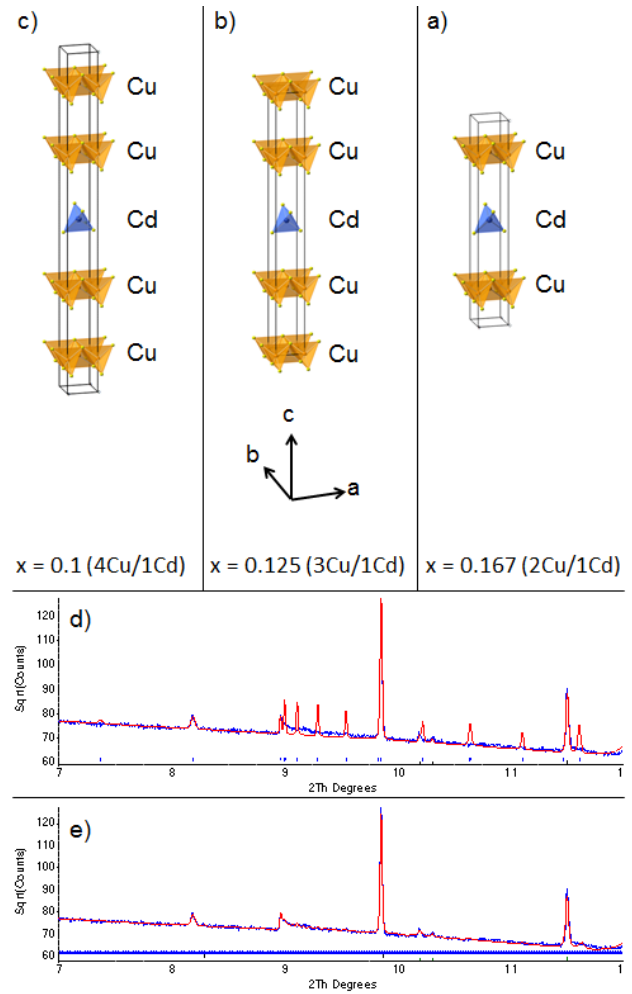


Figure 11. Structural models for (a)  $\text{La}_2\text{O}_2\text{Cu}_{1.33}\text{Cd}_{0.33}\text{Se}_2$  (2Cu/1Cd), (b)  $\text{La}_2\text{O}_2\text{Cu}_{1.50}\text{Cd}_{0.25}\text{Se}_2$  (3Cu/1Cd) and (c)  $\text{La}_2\text{O}_2\text{Cu}_{1.60}\text{Cd}_{0.20}\text{Se}_2$  (4Cu/1Cd), all space group  $P-4m2$ .  $\text{Cu}^{1+}$  cations are shown in orange,  $\text{Cd}^{2+}$  cations in blue and  $\text{Se}^{2-}$  anions in yellow.  $[\text{La}_2\text{O}_2]^{2+}$  layers are omitted for clarity. (d) and (e) show the Rietveld fit for  $x = 0.1$  with no faults and 0.05/0.50 *pa/pb* faults respectively. The  $2\theta$   $8.2^\circ$  peak has 1–0.4% of the strongest reflection.

## DISCUSSION

Our previous work on single-metal layered oxychalcogenides has shown that the combination of a rigid oxide layer and a more flexible chalcogenide layer can lead to structures with remarkable complexity and large superstructures in the *ab* plane.<sup>14, 15</sup> In this work we have shown that a similar level of complexity can be built into these materials along the stacking direction by using two metals, giving rise to the range of materials from 4Cd/1Cu to 1Cd/4Cu shown schematically in Figure 2. Whilst we use a conventional description in this work, these can all be described in terms of a superspace group  $P4/nmm(oog)soos$  [129.4]. The tendency to adopt ordered superstructures of this type is initially surprising, but again has its origin in the rigidity of the oxide layers in the *ab* plane. This rigidity forces two fixed Se–Se dimensions on the  $\text{MSe}_4$  tetrahedra, and the planar layers means that they can only adjust to coordinate a given transition metal by elongation along their  $S_4$  axis (parallel to *c*). Simple bond valence arguments<sup>75, 76</sup> for a  $\text{Cu}^{1+}$  or  $\text{Cd}^{2+}$  in this environment imply Se–Se layer distances of  $\sim 3.0$  and  $\sim 3.4$  Å respectively. This

large difference in geometry provides a strong driving force for segregation of Cu and Cd into separate layers.

Both our crystallographic models and stacking fault analyses show an initially counterintuitive arrangement of Cd sites in CdSe<sub>2</sub> layers separated by a Cu<sub>2</sub>Se<sub>2</sub> block. In pure La<sub>2</sub>O<sub>2</sub>CdSe<sub>2</sub> the Cd ordering pattern can be derived from the parent Cu structure in terms of a Z<sub>4</sub><sup>-</sup> ordering mode which leads to a checkerboard ordering within layers and adjacent layers with Cd positions offset by (½, ½) in the *ab* plane such that layers repeat in an ABAB sequence along *c*. This arrangement would be expected purely on electrostatic grounds and is retained within the Cd blocks of all our materials. Figure 6, however, shows that Cd positions are mirrored across the single Cu<sub>2</sub>Se<sub>2</sub> layers in the Cd-rich materials. As such, the Cd A(B)A stacking sequence [where (B) indicates the effective position of the Cu layer] is retained. We also find that the *pa* stacking fault for the *x* = 0.33 and *x* = 0.375 samples is best modelled such that Cd sites alternate across a double layer, again retaining the A(B)(A)B sequence through the fault. One possible explanation for this is that the *pa* fault occurs within column-like domains in a crystallite. The Cd ions immediately following a local double-Cu layer would then be in registry with other Cd sites within that layer following this type of fault. The only structure in

which the ABAB sequence is not followed is the *x* = 0.166 2Cu/1Cd composition. Since the *pb* type disorder is high in the Cu rich sequences, our observations are consistent with Cd preferring a mirrored configuration across multiple Cu layers.

The powder diffraction data show that there is significant long range order along the *c*-axis of these materials, with a relatively low probability of faults (*pa*) in the Cu/Cd sequence. There is also a strong tendency for Cd sites to adopt ordered positions in the *ab* plane in Cd-rich materials but that this tendency is reduced as the CdSe<sub>2</sub> layers become separated by more than 1 Cu<sub>2</sub>Se<sub>2</sub> layers. Stacking fault probabilities *pa* and *pb* are given in Figure 2. The different types of faults lead to the characteristic changes in superstructure peak shapes and intensities across the series shown in Figure 12.

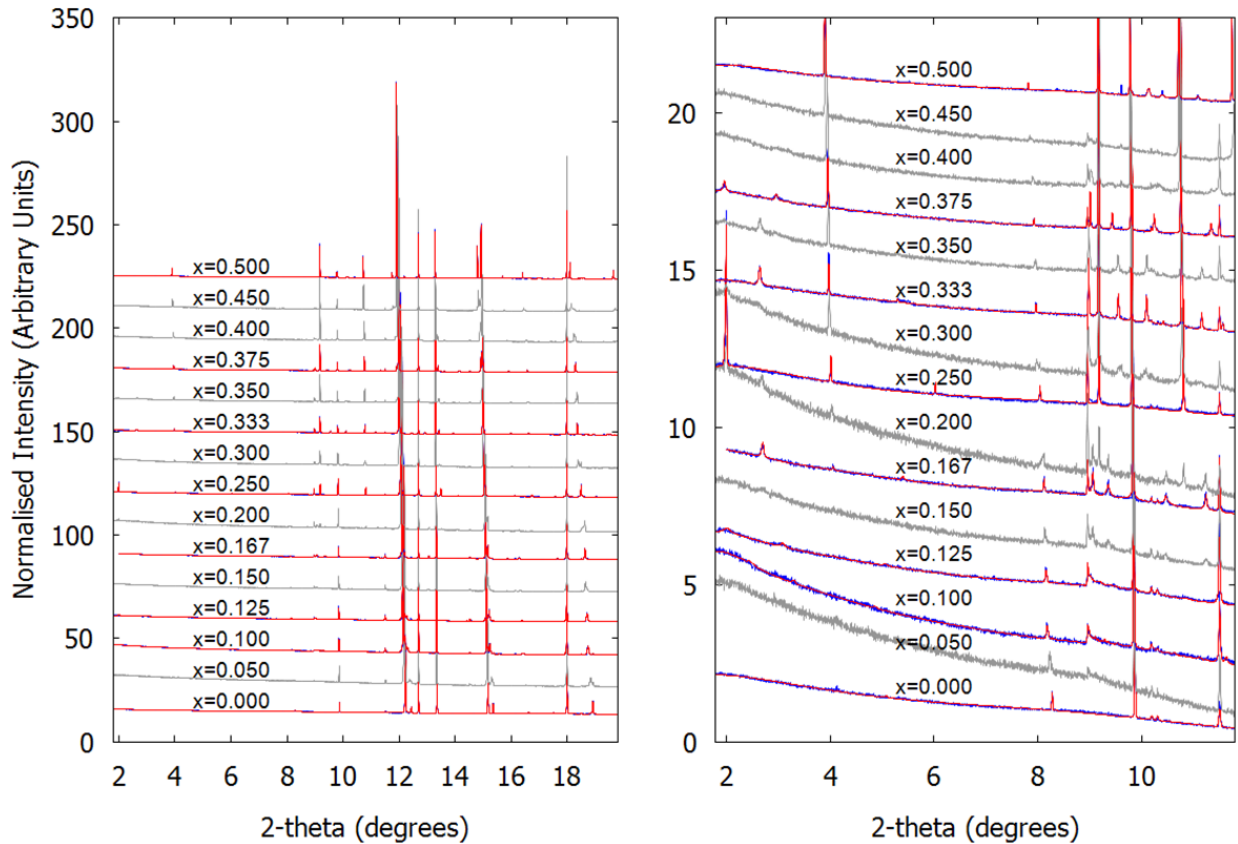


Figure 12. Rietveld fits for all compositions studied using the stacking approach. Left hand panel shows all data normalized on a 0–100 scale and offset vertically by 20 units for presentation. Right hand panel shows data over a low 2-theta range to emphasise the weak superstructure reflections which reveal metal ordering. Data sets are offset by 2 units along the y-axis. The differing backgrounds reflect different capillary packings. Rietveld fits of *x* = 0.167 and 0.125 are averages of 100 unique stacks.

## CONCLUSIONS

In conclusion, we show that we can take the design principle of combining rigid oxide blocks with more flexible chalcogenide blocks learnt from the 2D  $\text{La}_2\text{O}_3\text{MSe}_2$  infinitely flexible materials, and use them to produce cation-ordered materials over a large length scale in the 3<sup>rd</sup> dimension. This has allowed us to produce materials with stacks of electronically-interesting  $\text{Cu}_2\text{Se}_2$  layers where we can systematically change the number of adjacent layers and/or the separation between them in a controlled fashion. This gives access to a large new oxychalcogenide family which can potentially be doped to give p-type conductors related to the important  $\text{LaOCuSe}$  and  $\text{BiOCuSe}$  families. By using different metal chalcogenide layers we have the possibility to combine electronic and magnetically active layers in a controllable structural family.

We also show how materials with low and high-probability stacking faults can be properly analysed within the Rietveld method for the first time. This allows us to simultaneously extract structural (by refining atomic coordinates) and microstructural (by analysing stacking fault probabilities) information on our samples. The ability to correctly fit complex peak shapes with a small number of structurally meaningful parameters means that reflection intensities are correctly modelled, which is essential for accurate structural information or accurate quantitative analysis. The method we describe is entirely general and will be applicable to the wide range of materials that exhibit stacking faults. For example, we see important applications in battery materials such as  $\text{Li}_x\text{MO}_2$ <sup>33-36</sup>,  $\text{Na}_x\text{Fe}_{1/2}\text{Mn}_{1/2}\text{O}_2$ <sup>32</sup>,  $\text{Li}_2\text{FeSiO}_4$ <sup>31</sup> and  $\text{MnO}_2$ <sup>30</sup> where stacking faults are prevalent. Stacking fault Rietveld refinement will allow the accurate cation distributions, detailed structural information and quantitative analysis of *in-operando* systems needed for full understanding of their chemistry. Similar faulting precludes detailed structural studies of a range of important zeolites<sup>37-44</sup>. Other areas likely to benefit include materials with low temperature topotactic transformations<sup>77</sup>, intercalation/ion-exchange hosts, a variety of layered minerals<sup>78</sup>, and understanding the details and implications of hexagonal/cubic intergrowths in different forms of ice<sup>50, 51</sup>. Similar analysis will also be possible for layered magnetic systems, which often order in 2D or over short length scales prior to full 3D ordering.

## ASSOCIATED CONTENT

### Supporting Information

Supporting information document includes: table of sample colors, table of weight % of phases formed, graph showing the dependence of unit cell parameters on composition, graph showing the thickness of Se–Cu–Se and Se–Cd–Se layers from conventional Rietveld refinement, table of crystallographic information from conventional refinement, graph showing full width at half maximum of individual reflections in  $x = 0.33$  sample, tables showing dependence of  $R_{\text{wp}}$  on  $pa$  and  $pb$  for  $x = 0.33$ , 0.167 and 0.125 compositions, scatter plot showing  $R_{\text{wp}}$  for stacks with different numbers of  $pa$ -type and  $pb$ -type faults for  $x = 0.33$ , 0.167 and 0.125 compositions, CIF files for  $x = 0.25$ , 0.167 and 0.33, an annotated TOPAS input file and data file for the refinement of Figure 3b.

## AUTHOR INFORMATION

### Corresponding Author

\*E-mail: [john.evans@durham.ac.uk](mailto:john.evans@durham.ac.uk)

### Present Addresses

\*Chun-Hai Wang - School of Chemistry, The University of Sydney, NSW 2006 Australia

§Hannah E. Johnston - University of Edinburgh, Joseph Black Building, David Brewster Road, Edinburgh, Scotland EH9 3FJ

### Notes

The authors declare no competing financial interests.

## ACKNOWLEDGMENT

We thank EPSRC for funding (EP/J011533/1). Powder diffraction data were collected on the Powder Diffraction beamline at the Australian synchrotron. We thank Ivana Evans, Matthew Tate, Nicola Scarlett and Garry McIntyre for assistance with data collections. JSOE would like to thank ANSTO for a visiting position during which part of this research was performed.

## REFERENCES

- Kamihara, Y.; Watanabe, T.; Hirano, M.; Hosono, H., Iron-Based Layered Superconductor  $\text{La}[\text{O}_{1-x}\text{F}_x]\text{FeAs}$  ( $x = 0.05\text{--}0.12$ ) with  $T_c = 26$  K. *J. Am. Chem. Soc.* **2008**, *130*, (11), 3296-3297.
- Hosono, H.; Kuroki, K., Iron-Based Superconductors: Current Status of Materials and Pairing Mechanism. *Phys. C (Amsterdam, Neth.)* **2015**, *514*, 399-422.
- Phelan, W. A.; Wallace, D. C.; Arpino, K. E.; Neilson, J. R.; Livi, K. J.; Seabourne, C. R.; Scott, A. J.; McQueen, T. M., Stacking Variants and Superconductivity in the Bi-O-S System. *J. Am. Chem. Soc.* **2013**, *135*, (14), 5372-5374.
- Singh, S. K.; Kumar, A.; Gahtori, B.; Shruti; Sharma, G.; Patnaik, S.; Awana, V. P. S., Bulk Superconductivity in Bismuth Oxysulfide  $\text{Bi}_4\text{O}_4\text{S}_3$ . *J. Am. Chem. Soc.* **2012**, *134*, (40), 16504-16507.
- Zhao, L.; Berardan, D.; Pei, Y.; Byl, C.; Pinsard-Gaudart, L.; Dragoë, N.,  $\text{Bi}_x\text{Sr}_x\text{CuSeO}$  Oxyselenides as Promising Thermoelectric Materials. *Appl. Phys. Lett.* **2010**, *97*, 092118-092121.
- Luu, S. D.; Vaquero, P., Synthesis, Structural Characterisation and Thermoelectric Properties of  $\text{Bi}_{1-x}\text{Pb}_x\text{OCuSe}$ . *J. Mater. Chem. A* **2013**, *1*, (39), 12270-12275.
- Vaquero, P.; Al Orabi, R.; Luu, S.; Guélou, G.; Powell, A.; Smith, R.; Song, J.-P.; Wee, D.; Fornari, M., The Role of Copper in the Thermal Conductivity of Thermoelectric Oxychalcogenides: Do Lone Pairs Matter? *Phys. Chem. Chem. Phys.* **2015**, *17*, (47), 31735-31740.
- Liu, Y.; Zhao, L.-D.; Liu, Y.; Lan, J.; Xu, W.; Li, F.; Zhang, B.-P.; Berardan, D.; Dragoë, N.; Lin, Y.-H.; Nan, C.-W.; Li, J.-F.; Zhu, H., Remarkable Enhancement in Thermoelectric Performance of  $\text{BiCuSeO}$  by Cu Deficiencies. *J. Am. Chem. Soc.* **2011**, *133*, (50), 20112-20115.
- Bang, J.; Abboudi, M.; Abrams, B.; Holloway, P. H., Combustion Synthesis of Eu-, Tb- and Tm- Doped  $\text{Ln}_2\text{O}_2\text{S}$  ( $\text{Ln}=\text{Y}, \text{La}, \text{Gd}$ ) Phosphors. *J. Lumin.* **2004**, *106*, (3-4), 177-185.
- Clarke, S. J.; Denis, S. G.; Rutt, O. J.; Hill, T. L.; Hayward, M. A.; Hyett, G.; Gál, Z. A., Sodium Intercalation into the  $n = 2$  Ruddlesden-Popper Type Host  $\text{Y}_2\text{Ti}_2\text{O}_5\text{S}_2$ : Synthesis, Structure, and Properties of  $\alpha\text{-Na}_x\text{Y}_2\text{Ti}_2\text{O}_5\text{S}_2$  ( $0 < x \leq 1$ ). *Chem. Mater.* **2003**, *15*, (26), 5065-5072.
- Hyett, G.; Rutt, O. J.; Gal, Z. A.; Denis, S. G.; Hayward, M. A.; Clarke, S. J., Electronically Driven Structural Distortions in Lithium Intercalates of the  $n = 2$  Ruddlesden-Popper-Type Host  $\text{Y}_2\text{Ti}_2\text{O}_5\text{S}_2$ : Synthesis, Structure, and Properties of  $\text{Li}_x\text{Y}_2\text{Ti}_2\text{O}_5\text{S}_2$  ( $0 < x < 2$ ). *J. Am. Chem. Soc.* **2004**, *126*, (7), 1980-1991.
- Indris, S.; Cabana, J.; Rutt, O. J.; Clarke, S. J.; Grey, C. P., Layered Oxysulfides  $\text{Sr}_2\text{MnO}_2\text{Cu}_{2m-0.5}\text{S}_{m+1}$  ( $m = 1, 2$ , and  $3$ ) as Insertion Hosts for Li Ion Batteries. *J. Am. Chem. Soc.* **2006**, *128*, (41), 13354-13355.
- McCabe, E. E.; Free, D. G.; Evans, J. S. O., A New Iron Oxyselenide  $\text{Ce}_2\text{O}_2\text{FeSe}_2$ : Synthesis and Characterisation. *Chem. Commun.* **2011**, *47*, (4), 1261-1263.
- Wang, C.-H.; Ainsworth, C. M.; Gui, D.-Y.; McCabe, E. E.; Tucker, M. G.; Evans, I. R.; Evans, J. S. O., Infinitely Adaptive Transition Metal Oxychalcogenides: The Modulated Structures of  $\text{Ce}_2\text{O}_2\text{MnSe}_2$  and  $(\text{Ce}_{0.78}\text{La}_{0.22})_2\text{O}_2\text{MnSe}_2$ . *Chem. Mater.* **2015**, *27*, (8), 3121-3134.
- Ainsworth, C. M.; Wang, C.-H.; Johnston, H. E.; McCabe, E. E.; Tucker, M. G.; Brand, H. E. A.; Evans, J. S. O., Infinitely Adaptive Transition-Metal Ordering in  $\text{Ln}_2\text{O}_2\text{MSe}_2$ -Type Oxychalcogenides. *Inorg. Chem.* **2015**, *54*, (15), 7230-7238.
- Hiramatsu, H.; Yanagi, H.; Kamiya, T.; Ueda, K.; Hirano, M.; Hosono, H., Crystal Structures, Optoelectronic Properties, and Electronic Structures of Layered Oxychalcogenides  $\text{MCuOCh}$  ( $\text{M} = \text{Bi}, \text{La}$ ;  $\text{Ch} = \text{S}, \text{Se}, \text{Te}$ ): Effects of Electronic Configurations of  $\text{M}^{3+}$  Ions. *Chem. Mater.* **2008**, *20*, (1), 326-334.
- Ueda, K.; Takafuji, K.; Hiramatsu, H.; Ohta, H.; Kamiya, T.; Hirano, M.; Hosono, H., Electrical and Optical Properties and Electronic Structures of  $\text{LnCuOS}$  ( $\text{Ln} = \text{La}\text{--}\text{Nd}$ ). *Chem. Mater.* **2003**, *15*, (19), 3692-3695.
- Hiramatsu, H.; Kamiya, T.; Tohei, T.; Ikenaga, E.; Mizoguchi, T.; Ikuhara, Y.; Kobayashi, K.; Hosono, H., Origins of Hole Doping and Relevant Optoelectronic Properties of Wide Gap p-Type Semiconductor,  $\text{LaCuOSe}$ . *J. Am. Chem. Soc.* **2010**, *132*, (42), 15060-15067.
- Vajenine, G. V.; Hoffmann, R., Compounds Containing Copper-Sulfur Layers: Electronic Structure, Conductivity, and Stability. *Inorg. Chem.* **1996**, *35*, (2), 451-457.
- Ueda, K.; Inoue, S.; Hirose, S.; Kawazoe, H.; Hosono, H., Transparent p-Type Semiconductor:  $\text{LaCuOS}$  Layered Oxysulfide. *Appl. Phys. Lett.* **2000**, *77*, (17), 2701-2703.
- Hiramatsu, H.; Ueda, K.; Ohta, H.; Kamiya, T.; Hirano, M.; Hosono, H., Excitonic Blue Luminescence from p- $\text{LaCuOSe}/n\text{-InGaZn}_5\text{O}_8$  Light-Emitting Diode at Room Temperature. *Appl. Phys. Lett.* **2005**, *87*, (21), 211107/1-211107/3
- Ijjaali, I.; Mitchell, K.; Haynes, C. L.; McFarland, A. D.; Van Duyne, R. P.; Ibers, J. A., Synthesis, Crystal Structure, and Optical Properties of  $\text{CeMn}_{0.5}\text{OSe}$ . *J. Solid State Chem.* **2003**, *176*, (1), 170-174.
- Hiramatsu, H.; Ueda, K.; Kamiya, T.; Ohta, H.; Hirano, M.; Hosono, H., Synthesis of Single-Phase Layered Oxychalcogenide  $\text{La}_2\text{CdO}_2\text{Se}_2$ : Crystal Structure, Optical and Electrical Properties. *J. Mater. Chem.* **2004**, *14*, (19), 2946-2950.
- Tuxworth, A. J.; McCabe, E. E.; Free, D. G.; Clark, S. J.; Evans, J. S. O., Structural Characterization and Physical Properties of the New Transition Metal Oxyselenide  $\text{La}_2\text{O}_2\text{ZnSe}_2$ . *Inorg. Chem.* **2013**, *52*, (4), 2078-2085.

25. Ainsworth, C. M.; Wang, C. H.; Tucker, M. G.; Evans, J. S. O., Synthesis, Structural Characterization, and Physical Properties of the New Transition Metal Oxyselelide  $Ce_2O_2ZnSe_2$ . *Inorg. Chem.* **2015**, 54, (4), 1563-1571.
26. Peschke, S.; Nitsche, F.; Johrendt, D., Flux Synthesis, Modulated Crystal Structures, and Physical Properties of  $REMn_{0.5}SeO$  (RE = La, Ce). *Z. Anorg. Allg. Chem.* **2015**, 641, (3-4), 529-536.
27. Nitsche, F.; Niklaus, R.; Johrendt, D., New Polymorphs of  $RE_2FeSe_2O_2$  (RE = La, Ce). *Z. Anorg. Allg. Chem.* **2014**, 640, (14), 2897-2902.
28. Treacy, M. M. J.; Newsam, J. M.; Deem, M. W., A General Recursion Method for Calculating Diffracted Intensities from Crystals Containing Planar Faults. *Proc. R. Soc. A* **1991**, 433, (1889), 499-520.
29. Leoni, M., Diffraction Analysis of Layer Disorder. *Kristallogr.* **2008**, 223, (9), 561-568.
30. Chabre, Y.; Pannetier, J., Structural and Electrochemical Properties of the Proton Gamma- $MnO_2$  system. *Prog. Solid State Ch.* **1995**, 23, (1), 1-130.
31. Boulineau, A.; Sirisopanaporn, C.; Dominko, R.; Armstrong, A. R.; Bruce, P. G.; Masquelier, C., Polymorphism and Structural Defects in  $Li_2FeSiO_4$ . *Dalton Trans.* **2010**, 39, (27), 6310-6316.
32. Yabuuchi, N.; Kajiyama, M.; Iwatate, J.; Nishikawa, H.; Hitomi, S.; Okuyama, R.; Usui, R.; Yamada, Y.; Komaba, S., P2-type  $Na_xFe_{1/2}Mn_{1/2}O_2$  made from Earth-Abundant Elements for Rechargeable Na Batteries. *Nat. Mater.* **2012**, 11, (6), 512-517.
33. Lu, Z. H.; Dahn, J. R., In Situ X-Ray Diffraction Study of P2- $Na_{2/3}Ni_{1/3}Mn_{2/3}O_2$ . *J. Electrochem. Soc.* **2001**, 148, (11), A1225-A1229.
34. Bréger, J.; Jiang, M.; Dupré, N.; Meng, Y. S.; Shao-Horn, Y.; Ceder, G.; Grey, C. P., High-Resolution X-Ray Diffraction, DIFFaX, NMR and First Principles Study of Disorder in the  $Li_2MnO_3-Li[Ni_{1/2}Mn_{1/2}]O_2$  Solid Solution. *J. Solid State Chem.* **2005**, 178, (9), 2575-2585.
35. Croguennec, L.; Deniard, P.; Brec, R.; Lecerf, A., Nature of the Stacking Faults in Orthorhombic  $LiMnO_2$ . *J. Mater. Chem.* **1997**, 7, (3), 511-516.
36. Boulineau, A.; Croguennec, L.; Delmas, C.; Weill, F., Structure of  $Li_2MnO_3$  with Different Degrees of Defects. *Solid State Ionics* **2010**, 180, (40), 1652-1659.
37. Anderson, M. W.; Terasaki, O.; Ohsuna, T.; Philippou, A.; Mackay, S. P.; Ferreira, A.; Rocha, J.; Lidin, S., Structure of the Microporous Titanosilicate ETS-10. *Nature* **1994**, 367, (6461), 347-351.
38. Freyhardt, C. C.; Tsapatsis, M.; Lobo, R. F.; Balkus, K. J.; Davis, M. E., A High-Silica Zeolite with a 14-Tetrahedral-Atom Pore Opening. *Nature* **1996**, 381, (6580), 295-298.
39. Anderson, M. W.; Terasaki, O.; Ohsuna, T.; Malley, P. J. O.; Philippou, A.; Mackay, S. P.; Ferreira, A.; Rocha, J.; Lidin, S., Microporous Titanosilicate ETS-10 - A Structural Survey. *Philos. Mag. B* **1995**, 71, (5), 813-841.
40. Lobo, R. F.; Pan, M.; Chan, I.; Li, H. X.; Medrud, R. C.; Zones, S. I.; Crozier, P. A.; Davis, M. E., SSZ-26 and SSZ-33 - 2 Molecular-Sieves with Intersecting 10-Ring and 12-Ring Pores. *Science* **1993**, 262, (5139), 1543-1546.
41. Lobo, R. F.; Tsapatsis, M.; Freyhardt, C. C.; Khodabandeh, S.; Wagner, P.; Chen, C. Y.; Balkus, K. J.; Zones, S. I.; Davis, M. E., Characterization of the Extra-Large-Pore Zeolite UTD-1. *J. Am. Chem. Soc.* **1997**, 119, (36), 8474-8484.
42. Juttu, G. G.; Lobo, R. F., Characterization and Catalytic Properties of MCM-56 and MCM-22 Zeolites. *Microporous Mesoporous Mater.* **2000**, 40, (1-3), 9-23.
43. Lobo, R. F.; Tsapatsis, M.; Freyhardt, C. C.; Chan, I.; Chen, C. Y.; Zones, S. I.; Davis, M. E., A Model for the Structure of the Large-Pore Zeolite SSZ-31. *J. Am. Chem. Soc.* **1997**, 119, (16), 3732-3744.
44. Willhammar, T.; Sun, J.; Wan, W.; Oleynikov, P.; Zhang, D.; Zou, X.; Moliner, M.; Gonzalez, J.; Martínez, C.; Rey, F.; Corma, A., Structure and Catalytic Properties of the Most Complex Intergrown Zeolite ITQ-39 Determined by Electron Crystallography. *Nat. Chem.* **2012**, 4, (3), 188-194.
45. Balogh, L.; Ungar, T.; Zhao, Y.; Zhu, Y. T.; Horita, Z.; Xu, C.; Langdon, T. G., Influence of Stacking-Fault Energy on Microstructural Characteristics of Ultrafine-Grain Copper and Copper-Zinc Alloys. *Acta Mater.* **2008**, 56, (4), 809-820.
46. Sebastian, M. T.; Krishna, P., *Random, Non-random, and Periodic Faulting in Crystals*. Gordon and Breach Science Publishers: 1994.
47. Ufer, K.; Kleeberg, R.; Bergmann, J.; Dohrmann, R., Rietveld Refinement of Disordered Illite-Smectite Mixed-Layer Structures by a Recursive Algorithm. II: Powder-Pattern Refinement and Quantitative Phase Analysis. *Clays Clay Miner.* **2012**, 60, (5), 535-552.
48. Ufer, K.; Kleeberg, R.; Bergmann, J.; Dohrmann, R., Rietveld Refinement of Disordered Illite-Smectite Mixed-Layer Structures by a Recursive Algorithm. I: One-Dimensional Patterns. *Clays Clay Miner.* **2012**, 60, (5), 507-534.
49. Németh, P.; Garvie, L. A.; Aoki, T.; Dubrovinskaya, N.; Dubrovinsky, L.; Buseck, P. R., Lonsdaleite is Faulted and Twinned Cubic Diamond and does Not Exist as a Discrete Material. *Nat. Commun.* **2014**, 5.
50. Salzmann, C. G.; Murray, B. J.; Shephard, J. J., Extent of Stacking Disorder in Diamond. *Diam. Relat. Mater.* **2015**, 59, 69-72.
51. Malkin, T. L.; Murray, B. J.; Salzmann, C. G.; Molinero, V.; Pickering, S. J.; Whale, T. F., Stacking Disorder in Ice I. *Phys. Chem. Chem. Phys.* **2015**, 17, (1), 60-76.
52. Fogg, A. M.; Evans, J. S. O.; O'Hare, D., Crystal Structure of Beta-MNX (M = Zr, Hf, X = Cl, Br). *Chem. Commun.* **1998**, (20), 2269-2270.

53. Stampfl, C.; Van de Walle, C. G., Energetics and Electronic Structure of Stacking Faults in AlN, GaN, and InN. *Phys. Rev. B* **1998**, *57*, (24), R15052-R15055.
54. Liu, R.; Bell, A.; Ponce, F. A.; Chen, C. Q.; Yang, J. W.; Khan, M. A., Luminescence from Stacking Faults in Gallium Nitride. *Appl. Phys. Lett.* **2005**, *86*, (2), 021908.
55. Anselmi-Tamburini, U.; Ohyanagi, M.; Munir, Z. A., Modeling Studies of the Effect of Twins on the X-Ray Diffraction Patterns of Boron Carbide. *Chem. Mater.* **2004**, *16*, (22), 4347-4351.
56. Anselmi-Tamburini, U.; Munir, Z. A.; Kodera, Y.; Imai, T.; Ohyanagi, M., Influence of Synthesis Temperature on the Defect Structure of Boron Carbide: Experimental and Modeling Studies. *J. Am. Ceram. Soc.* **2005**, *88*, (6), 1382-1387.
57. Palosz, B.; Stelmakh, S.; Gierlotka, S., Refinement of Polycrystalline Disordered Cubic Silicon-Carbide by Structure Modeling and X-Ray-Diffraction Simulation. *Z. Kristallogr.* **1995**, *210*, (10), 731-740.
58. Nguyen, P.; Sleight, A.; Roberts, N.; Warren, W., Modeling of Extended Defects in the Vanadium Phosphate Catalyst for Butane Oxidation,  $(VO)_2P_2O_7$ . *J. Solid State Chem.* **1996**, *122*, (2), 259-265.
59. Rajamathi, M.; Kamath, P. V.; Seshadri, R., Polymorphism in Nickel Hydroxide: Role of Interstratification. *J. Mater. Chem.* **2000**, *10*, (2), 503-506.
60. Rajamathi, M.; Kamath, P. V.; Seshadri, R., Chemical Synthesis of Alpha-Cobalt Hydroxide. *Mater. Res. Bull.* **2000**, *35*, (2), 271-278.
61. Jayashree, R. S.; Kamath, P. V.; Subbanna, G. N., The Effect of Crystallinity on the Reversible Discharge Capacity of Nickel Hydroxide. *J. Electrochem. Soc.* **2000**, *147*, (6), 2029-2032.
62. Radha, A. V.; Kamath, P. V.; Shivakumara, C., Conservation of Order, Disorder, and "Crystallinity" during Anion-Exchange Reactions among Layered Double Hydroxides (LDHs) of Zn with Al. *J. Phys. Chem. B* **2007**, *111*, (13), 3411-3418.
63. Coelho, A. A., Indexing of Powder Diffraction Patterns by Iterative Use of Singular Value Decomposition. *J. Appl. Crystallogr.* **2003**, *36*, 86-95.
64. Coelho, A. A., *TOPAS Academic: General Profile and Structure Analysis Software for Powder Diffraction Data*. 5th ed.; Bruker AXS: Karlsruhe, Germany: 2012.
65. Coelho, A. A.; Evans, J. S. O.; Evans, I. R.; Kern, A.; Parsons, S., The TOPAS Symbolic Computation System. *Powder Diffr.* **2011**, *26*, S22-S25.
66. Warren, B. E., X-Ray Diffraction in Random Layer Lattices. *Phys. Rev.* **1941**, *59*, (9), 693-698.
67. Proffen, T.; Neder, R. B., *Diffuse Scattering and Defect Structure Simulations: A Cook Book Using the Program DISCUS*. Oxford University Press: Oxford, 2008.
68. Leoni, M.; Gualtieri, A. F.; Roveri, N., Simultaneous Refinement of Structure and Microstructure of Layered Materials. *J. Appl. Crystallogr.* **2004**, *37*, 166-173.
69. Casas-Cabanas, M.; Rodriguez-Carvajal, J.; Canales-Vazquez, J.; Lalignat, Y.; Lacorre, P.; Palacin, M. R., Microstructural characterisation of battery materials using powder diffraction data: DIFFaX, FAULTS and SH-FullProf approaches. *J. Power Sources* **2007**, *174*, (2), 414-420.
70. Ufer, K.; Roth, G.; Kleeberg, R.; Stanjek, H.; Dohrmann, R.; Bergmann, J., Description of X-Ray Powder Pattern of Turbostratically Disordered Layer Structures with a Rietveld Compatible Approach. *Z. Kristallogr.* **2004**, *219*, (9), 519-527.
71. Wang, X. D.; Li, J.; Hart, R. D.; van Riessen, A.; McDonald, R., Quantitative X-Ray Diffraction Phase Analysis of Poorly Ordered Nontronite Clay in Nickel Laterites. *J. Appl. Crystallogr.* **2011**, *44*, 902-910.
72. Bette, S.; Dinnebier, R. E.; Freyer, D., Structure Solution and Refinement of Stacking-Faulted NiCl(OH). *J. Appl. Crystallogr.* **2015**, *48*, 1706-1718.
73. Shannon, R., Revised Effective Ionic Radii and Systematic Studies of Interatomic Distances in Halides and Chalcogenides. *Acta Crystallogr. A* **1976**, *32*, (5), 751-767.
74. Her, J.-H.; Stephens, P. W.; Gao, Y.; Soloveichik, G. L.; Rijssenbeek, J.; Andrus, M.; Zhao, J.-C., Structure of Unsolvated Magnesium Borohydride  $Mg(BH_4)_2$ . *Acta Crystallogr. B* **2007**, *63*, 561-568.
75. Brese, N. E.; O'Keeffe, M., Bond-Valence Parameters for Solids. *Acta Crystallogr. B* **1991**, *47*, (2), 192-197.
76. Brown, I. D., Recent Developments in the Methods and Applications of the Bond Valence Model. *Chem. Rev.* **2009**, *109*, (12), 6858-6919.
77. Hayward, M. A.; Green, M. A.; Rosseinsky, M. J.; Sloan, J., Sodium Hydride as a Powerful Reducing Agent for Topotactic Oxide Deintercalation: Synthesis and Characterization of the Nickel(I) Oxide  $LaNiO_2$ . *J. Am. Chem. Soc.* **1999**, *121*, (38), 8843-8854.
78. Bellotto, M.; Rebours, B.; Clause, O.; Lynch, J.; Bazin, D.; Elkaim, E., A Reexamination of Hydrotalcite Crystal Chemistry. *J. Phys. Chem.* **1996**, *100*, (20), 8527-8534.
-

